ZIF-8 Template-Assisted Synthesis of Polyimide-Derived Nitrogen-Oxygen Co-doped Porous Carbon Microspheres for Supercapacitors

Xin Zhou[a], Juan Yu[a], Pei Huang[a], and Xiaodong Wang[a],*

*[a]State Key Laboratory of Materials-Oriented Chemical Engineering, College of Chemical Engineering,
Nanjing Tech University, Nanjing, 211816 China*
***e-mail: wangxd1188@njtech.edu.cn**

Received December 28, 2023; revised February 1, 2024; accepted March 1, 2024

Abstract—Nitrogen-oxygen co-doped porous carbon microspheres were synthesized through hydrothermal and carbonization processes using polyimide (PI) as the carbon precursor and a nitrogen-oxygen source. ZIF-8 was also used as the template. When the carbonization temperature reached 800°C, the porous carbon microspheres displayed a unique 3D sea urchin-like morphology, a high specific surface area (782.3 m^2/g), and good nitrogen and oxygen doping contents (6.62 and 11.92 at %, respectively). Electrochemical testing showed that when the scanning rate was 0.5 A/g, the material achieved a specific capacitance of 330.5 F/g, and the capacitance retention rate of the electrode material was 73.5% when the current density reached 10 A/g. Furthermore, the symmetrical supercapacitor assembled with this electrode had an operating voltage window that extended to 1.8 V and provided an energy density of 20.5 W h/kg at a power density of 400 W/kg. This method of preparing high performance nitrogen-oxygen co-doped carbon electrode materials provides an idea for the application of insulating polymers in the field of energy storage.

INTRODUCTION

The overconsumption of oil has led to environmental contamination and energy deficits, highlighting the need to promote sustainable and renewable energy sources. It is also essential to improve effective methods for energy conversion and storage [1]. Supercapacitors are widely regarded as efficient and reliable energy storage devices owing to their benefits of fast charging and discharging and good cycle stability [2, 3]. Electrode materials in supercapacitors are typically assumed the key to achieving high-performance energy storage. Compared with electrode materials, porous carbon materials have the benefits of low cost, good chemical stability, and a tunable pore structure, which offer a great deal of interest for use in the supercapacitor industry [4–6].

Current design based on porous carbon materials focuses mainly on modifying the morphology [7, 8]. The pore structure and chemistry of metal-organic frameworks (MOFs) can be designed and customized for various applications in electrochemical energy storage [9, 10]. Zeolitic imidazole frameworks (ZIF-8), as a representative MOF, has a three-dimensional structure, excellent thermal stability, and a high specific surface area. Therefore, researchers often utilize ZIF-8 as a template for the synthesis of nanoporous carbon materials [11–14]. However,

porous carbon materials tend to exhibit electrical double-layer capacitance behavior, resulting in low specific capacitance. Doping with heteroatoms (nitrogen, oxygen, fluorine, etc.) can alter the distribution of the electron cloud in carbon materials, thereby creating new active sites. It is beneficial for enhancing capacitance performance [15]. And the heteroatoms have lone electron pairs, which can not only be used as carriers to promote the migration of electrons, thus changing the spatial structure of the carbon layer, but also form hydrogen bonds with water [16–18]. This greatly improves the hydrophilicity of the material, which is conducive to improving cycling stability. Among the many heteroatoms, nitrogen doping induces polarization in sp^2-hybridized carbon networks and affects the physical properties of carbon materials. Oxygen doping can heighten the infiltration of electrolyte into electrode materials, thereby improving the cycling stability of porous carbon materials [19]. Therefore, nitrogen-oxygen co-doping has gained much attention and application in energy storage systems [20–22]. Polyimides (PI) with controlled molecular structures can be synthesized from a wide range of monomers, where nitrogen (N) and oxygen (O) atoms can induce the generation of additional pseudo-capacitance. The nitrogen and carbon atoms in the polyimide carbon skeleton have similar atomic

Fig. 1. Diagrammatic representation of the procedure for preparing porous carbon microspheres.

radii, making it easier to exchange carbon atoms in the carbon network during high-temperature carbonization. This greatly reduces the energy required for the doping process. And compared to other polymers, the carbonization process of PI is relatively simple, with a high carbon yield, making it one of the most potential carbon precursors.

Here, we provided a straightforward and synthesis technique. Porous carbon microspheres (PZ-C) were prepared from polyimide and ZIF-8 through hydrothermal and carbonization processes. Polyimide, as a carbon matrix skeleton, helps to establish the electron transport network, which ensures that the electrodes have excellent electrical conductivity. ZIF-8 acts as a sacrificial template and pore-forming agent, promoting the formation of three-dimensional porous carbon microsphere structures from PI/ZIF-8 (PZ) [23]. In addition, a significant amount of nitrogen and oxygen is retained in the polyimide backbone as a source of nitrogen and oxygen during polyimide carbonization [24]. This work can provide new ideas for the preparation and modification of supercapacitor electrode materials, making the practical application of green, efficient, and clean energy possible.

EXPERIMENTAL

Materials

2-Methylimidazole, and 4,4'-oxidianiline (ODA) were bought from Suzhou Yacoo Chemical Reagent Co. Ltd. Pyromellitic dianhydride (PMDA), Polyvinylidene fluoride (PVDF), Zn (CH$_3$COO)$_2$·2H$_2$O, methanol, and N,N-dimethylacetamide (DMAc) were bought from Nanjing Longsha Chemical Reagent Co. Ltd.

Syntheses and Preparations

A diagrammatic representation of the procedure for preparing porous carbon microspheres is shown in Fig. 1.

Synthesis of ZIF-8

1.75 g Zn (CH$_3$COO)$_2$·2H$_2$O and 2.64 g 2-methylimidazole were dissolved in methanol, respectively. After quickly combining the two solutions, they were left to stand for 24 h. To get ZIF-8, the combined solution was lastly cleaned with methanol and dried for 10 h at 90°C.

Synthesis of PI/ZIF-8(PZ)

Specifically, 0.8615 g ODA and 0.09 g ZIF-8 were dissolved in 37 mL DMAC, followed by slowly adding 0.936 g PMDA. After agitating for 10 h, the PAA/ZIF-8 solution was obtained. To obtain yellow PI/ZIF-8 powder, the prepared PAA/ZIF-8 solution was then moved to the Teflon-lined steel autoclave and hydrothermally heated at 180°C for 10 h. This sample was named PZ. For comparison, pure PI without adding ZIF-8 was prepared using the same process.

Synthesis of PI/ZIF-8-C(PZ-C)

The PZ powder was carbonized under nitrogen protection at 800°C for 2 h. The collected carbon was then washed with a hydrochloric acid solution (3.0 M). The obtained carbon material was named PZ-C, with the different samples carbonized at 700, 800, and 900°C named PZ-C-700, PZ-C-800, and PZ-C-900, respectively. PI-C-800 and Z8-C-800 were obtained through the same carbonation process.
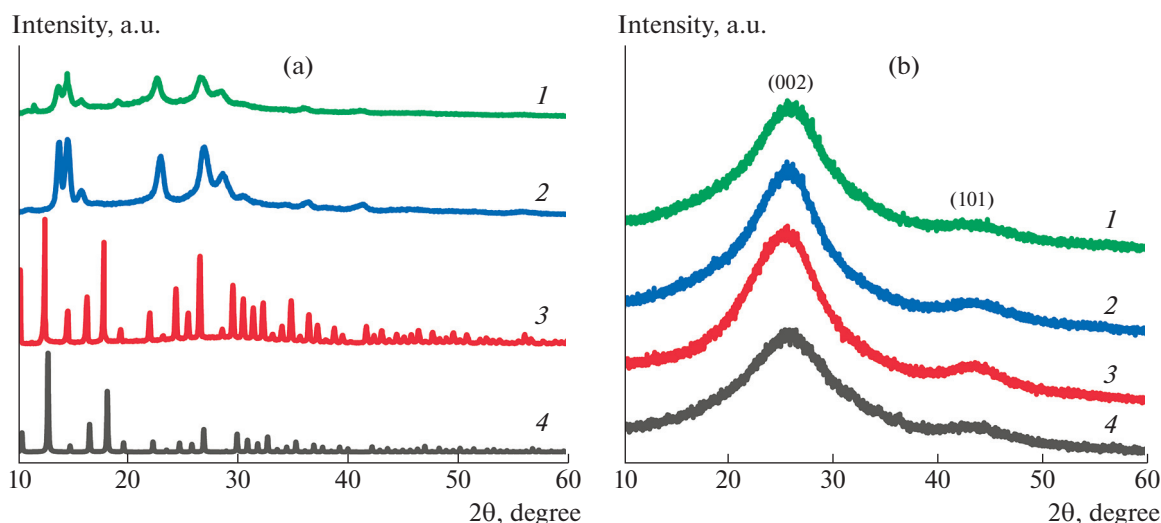
Fig. 2. (a) XRD pattern of (*1*) PZ, (*2*) PI, (*3*) ZIF-8, (*4*) simulate ZIF-8. (b) XRD pattern of (*1*) PZ-C-700, (*2*) PZ-C-800, (*3*) PZ-C-900, (*4*) PI-C-800.

Material Characterization

The chemical components, graphitic structure, and morphology were characterized by X-ray photoelectron spectroscopy (XPS Axis Supra), Raman spectroscopy (Raman Labram HR), scanning electron microscope (SEM S4800), and X-ray diffractometer (XRD Advance), respectively. The specific surface areas were calculated using the Brunauer-Emmett-Teller (BET) method, and pore size distributions were calculated by the Barrette–Joynere–Halenda (BJH) model.

Electrochemical Performance Evaluation

The active material, conductive carbon black, and PVDF were combined at a mass ratio of 8 : 1 : 1 and placed in the mortar to be ground evenly, then the appropriate amount of DMAc was added to formulate the slurry and ultrasonicated for 60 min to mix the slurry evenly. To create the electrode sheet, the combined electrode material was equally applied to the carbon cloth that had been created, and it was dried for 6 h at 70°C. Electrochemical performance testing was carried out using a three-electrode configuration, a CHI 660E electrochemical workstation, and 6M KOH as the electrolyte.

RESULTS AND DISCUSSION

Figure 2a displays the XRD patterns of ZIF-8, PI, and PZ. The findings demonstrate that there is a strong correlation between the diffraction peaks of ZIF-8 and conventional analog peaks. The peaks at 10.3°, 12.5°, 16.4°, and 17.8° are attributed to the (002), (112), (013), and (222) crystal faces of ZIF-8, respectively [25]. The characteristic peaks of PI show several sharp and strong peaks in the range of $2\theta = 15°$ to 34°, indicating that PI has a regular structure and high crystallinity [26]. The PZ composite material exhibits two small peaks at 11.6° and 14.6°, belonging to the (112) and (022) crystal faces of ZIF-8. The distinct peaks of PI for the PZ composites remain visible, suggesting that ZIF-8 does not alter the crystal structure. Figure 2b displays the PZ-Cs XRD patterns. The two broad peaks near $2\theta = 25°$ and 43° correspond to the crystal planes (002) and (100) of the graphene layer stacked with the carbon material, respectively. It shows the material undergoes graphitization at high temperatures [27]. And it can be found that the peak of weak diffraction of graphite carbon (100) increases with the increase in temperature, suggesting that the sample's degree of graphitization increased with temperature. This is conducive to expanding the electrical conductivity of the materials and reducing internal resistance.

Figure 3 displays the materials' Raman spectra, where a representative D band at 1350 cm^{-1} is linked to disordered carbon, while a representative G band at 1580 cm^{-1} is linked to graphitic carbon, proving that the material possesses a disordered structure and a degree of graphitization. It is evident that the I_D/I_G ratio of PZ-Cs increases with growing temperature, indicating a higher flaw ratio in the disordered carbon matrix [28]. This may be due to the increase in temperature, which causes a change in the carbon network structure within the material. Consequently, there is an increase in the disorganized framework of the carbon material.

Figures 4a and 4d show that the ZIF-8 crystals have a rhombic dodecahedral morphology with a smooth outer surface. Figures 4b and 4e display PI as a flower-like spherical structure composed of multiple 2D
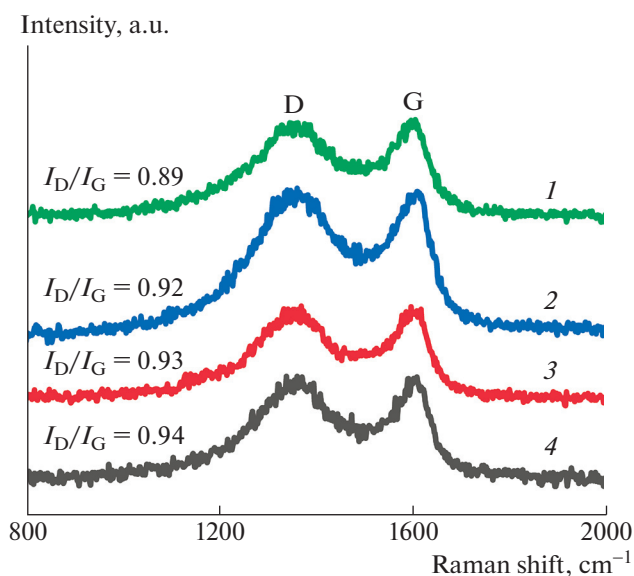
Intensity, a.u.

$I_D/I_G = 0.89$

$I_D/I_G = 0.92$

$I_D/I_G = 0.93$

$I_D/I_G = 0.94$

Fig. 3. Raman spectra of (*1*) PZ-C-700, (*2*) PZ-C-800, (*3*) PZ-C-900, (*4*) PI-C-800.

nanosheets. As shown in Figs. 4c and 4f, the PZ displays a porous spherical structure with sphere diameters ranging from 3 to 5 μm, and ZIF-8 is distributed around the microspheres. This may be due to the fact that ZIF-8 disrupts the molecular stacking of polymer chains under high temperature and pressure, which affects the self-assembly process of PI [24]. As shown in Figs. 4g–4l, it can be observed that PZ-C-700 exhibits a reticulated porous microsphere structure, with individual microspheres ranging in size from 5 to 6 μm. And the ZIF-8 crystals no longer maintain their rhombic dodecahedral morphology. This is because the organic ligands in the ZIF-8 backbone undergo pyrolysis under high-temperature conditions. PZ-C-800 has a sea urchin-like porous microsphere structure with an increased surface roughness. This unique sea urchin-like porous structure gives the material a large surface area. It also provides numerous channels for charge storage and transport [20]. The dimensions of the microspheres progressively decrease with the rise in carbonization temperature up to 900°C. The contraction of the polymer backbone during heat cracking might be the cause of this [23].

Table 1. Surface area and porous size distribution of samples

Samples	S_{BET}, m²/g	Pore volume, cm³/g	Pore size, nm
PI-C-800	621.9	0.64	4.46
PZ-C-700	679.9	0.69	4.03
PZ-C-800	782.3	0.76	3.40
PZ-C-900	917.1	1.10	4.70

Figure 5a displays the nitrogen sorption isotherms of the PI-C-800 and PZ-C-X samples. In all samples, the N₂ adsorption-dissorption temperature line rose sharply at low pressure, with a regression ring at P/P_o around 0.5–0.9, reflecting an adsorption curve of characteristics combined with type I and type IV. This suggests that the material has both medium and micropores [23]. As shown in Fig. 5b, the micropores of samples are concentrated between 0.4 and 2.0 nm, and the mesopores are concentrated between 3.0 and 6.0 nm. From Table 1 and Fig. 5b, it can be seen that the obtained carbon material has a multistage fractional pore structure dominated by mesopores and coexisting with micropores. A high surface area with a microporous structure is conducive to the double-stratified responses of supercapacitors. The mesopore reduces the path of electron transfer, and reduces the transmission resistance. The combination of two facilitates ion absorption on the surface of the electrode and electrolyte, increases charge shift response, and expands the material's capacity.

Table 1 shows the specific surface area and pore volume of the samples heightened as the carbonization temperatures increased. This may be due to the increase in the temperature of decomposition that leads to further thermal disintegration of the material. And with the addition of ZIF-8, PZ-C-800's pore volume and specific surface area rose to 0.76 cm³/g and 782.3 m²/g, respectively. It may be due to the decomposition and carbonization of ZIF-8 at high temperatures, where Zn in the structure is converted to ZnO. And these ZnO nanoparticles, which are generated, can be utilized as hard templates that are embedded in the carbon skeleton. These templates are then removed through acid etching to create the pore network [24]. When the temperature reached 800°C, ZnO underwent reduction to form Zn metal vapor due to the presence of generated C. The samples' porosity and specific surface area increased further as a outcome of this physical activation of the carbon matrix.

XPS measurement was utilized to ascertain the composition and surface elements of PZ-C carbon microspheres treated at different temperatures. According to Fig. 6a, C, N, and O are the primary constituents of the PZ carbon microspheres. According to Fig. 6b, the C1s fitting curves show four fitting peaks at 284.8, 286, 288.2, and 291.2 eV, which stand for C=C, C–O, C=O, and O–C=O, respectively. The fitted curves of O1s in Fig. 6c show the presence of oxygenated functional groups of C=O at 531.2 eV, C–OH at 533.3 eV, and –COOH at 537.2 eV. As shown in Fig. 6d, four nitrogen bonding configurations were found at 398.5, 400.2, 401.4, and 405.4 eV. They correspond to N-6, N-5, N-Q, and N-X, respectively. N-5 can donate electrons to carbon atoms, thereby providing additional pseudo-capacitance through Faraday redox reactions. Additionally, Nitrogen atoms rearrange during the carbonization
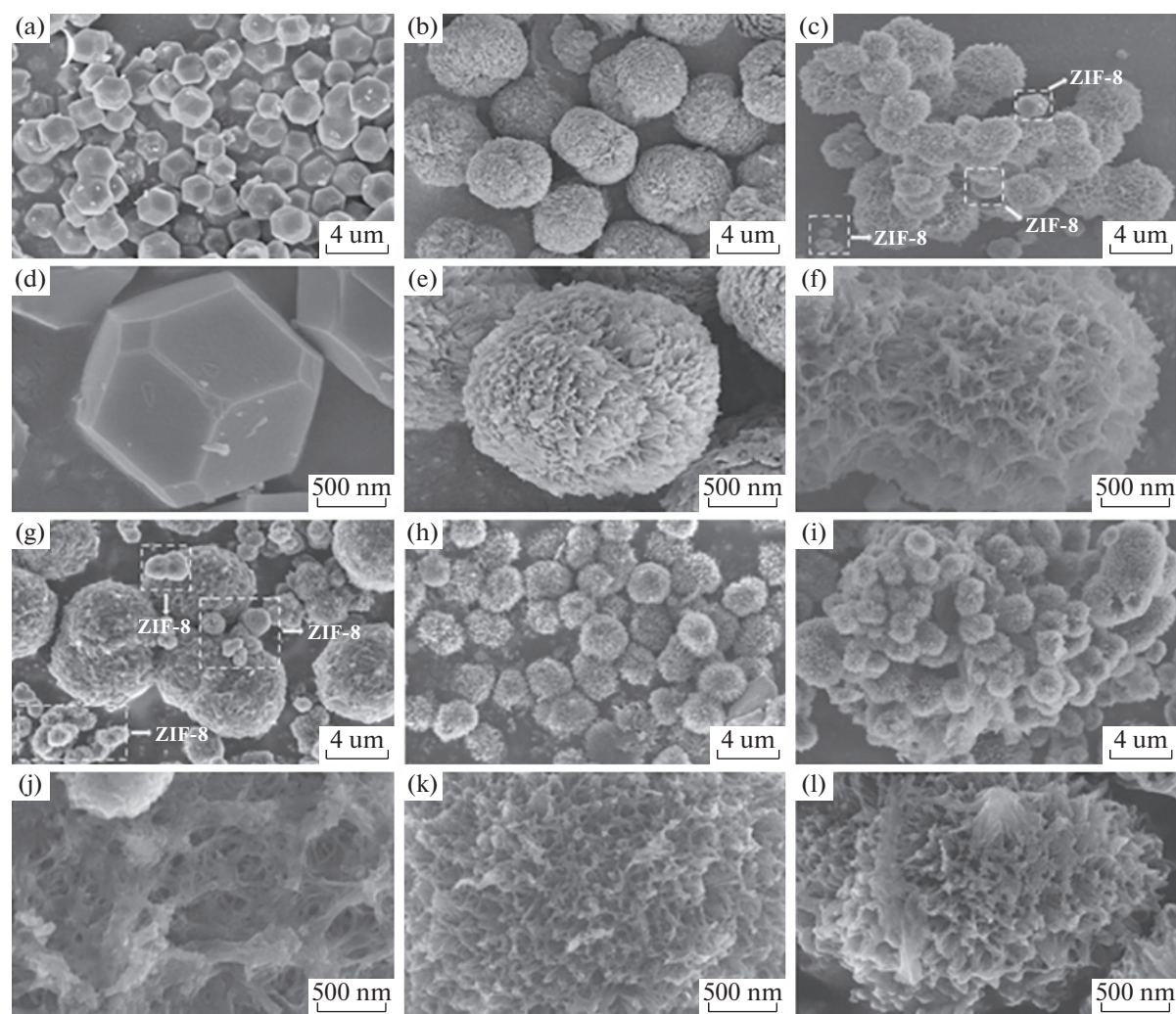
Fig. 4. SEM images of the (a, d) ZIF-8, (b, e) PI, (c, f) PZ, (g, j) PZ-C-700, (h, k) PZ-C-800 and (i, l) PZ-C-900 at different magnification.
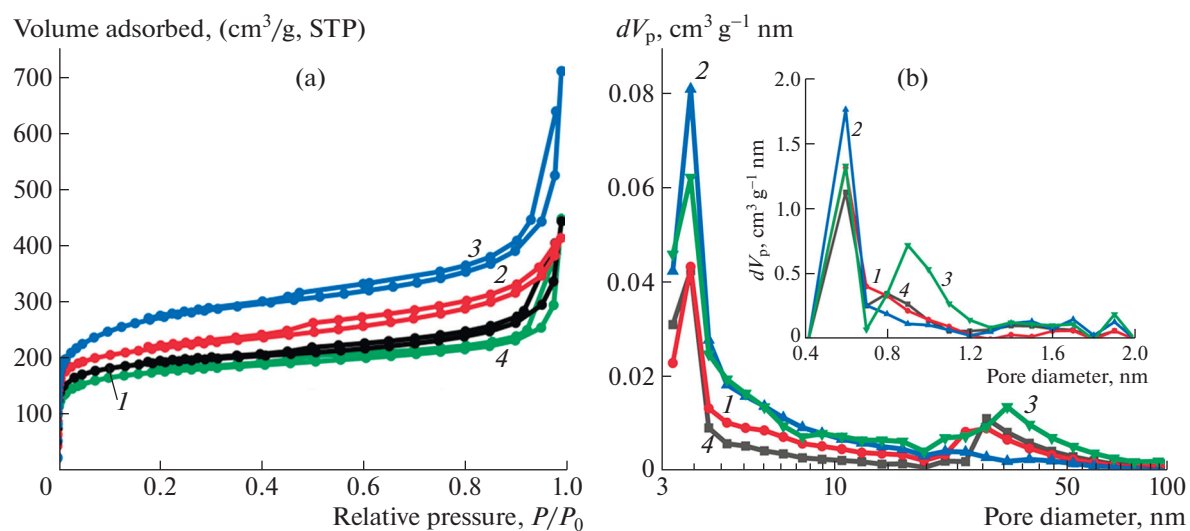

Fig. 5. (a) N$_2$ adsorption desorption isotherm, and (b) aperture distribution map of materials: (*1*) PZ-C-700, (*2*) PZ-C-800, (*3*) PZ-C-900, (*4*) PI-C-800.
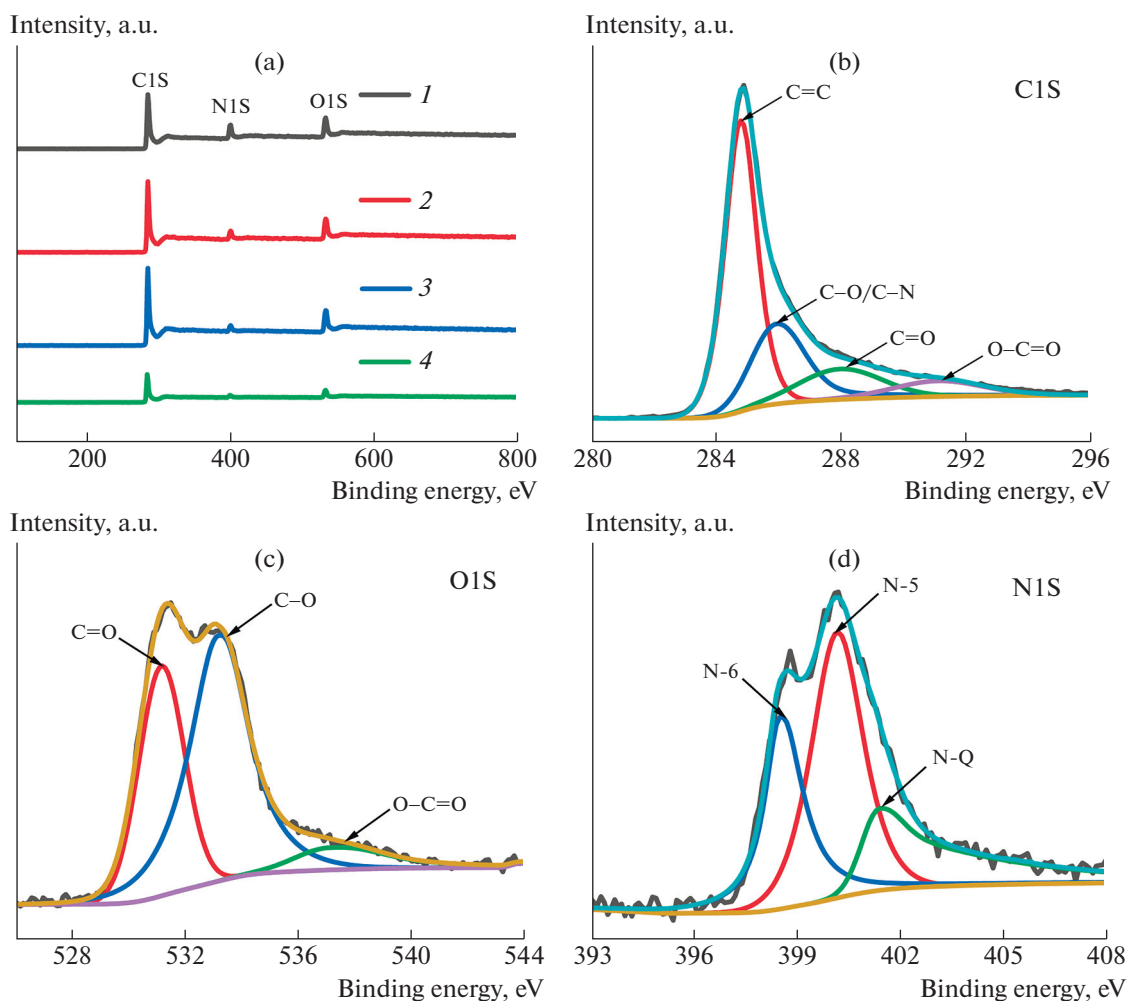
Fig. 6. (a) XPS survey spectra of (*1*) PZ-C-700, (*2*) PZ-C-800, (*3*) PZ-C-900, (*4*) PI-C-800. High-resolution XPS spectra with matching fitting findings for (b) C 1s, (c) N 1s, and (d) O 1s.

process to generate N-Q [22]. This rearrangement can alter the band structure of carbon materials, increase the mobility of electrons and holes, and serve as active sites for electrochemical reactions. As a consequence, it enhances the electronic conductivity and charge storage properties of carbon materials.

The surface element contents of the samples are given in Table 2. The relative content of carbon and oxygen elements in the samples increased significantly

Table 2. The corresponding surface element contents of samples

Samples	C, at %	N, at %	O, at %	Zn, at %
PI-C-800	83.76	4.70	11.54	0
PZ-C-700	75.73	12.18	11.91	0.18
PZ-C-800	81.37	6.62	11.92	0.09
PZ-C-900	83.46	4.00	12.47	0.07

with increasing carbonization temperatures. This is because the surface of the sample has developed flaws that reveal the carbon layer and functional groups that contain oxygen. The release of unstable nitrogen-containing molecules from the activated samples at high temperatures may be the cause of the drop in nitrogen content [20].

Electrochemical tests were conducted on carbon materials in a three-electrode system to examine their electrochemical properties. Figure 7a shows that all the CV curve shapes are approximately rectangular, among which the PZ-C-800 display the biggest CV curve area, indicating that the electrode has a large capacitance [29]. Figure 7b shows all highly symmetrical isosceles triangles, which means that these electrodes have good electrochemical. And the discharge time of PZ-C-800 is longer, demonstrating that the specific capacitance of PZ-C-800 is the biggest compared to other carbon materials. To observe the electrochemical resistance attributes of electrode materials, an exchange resistance evaluation of all samples is
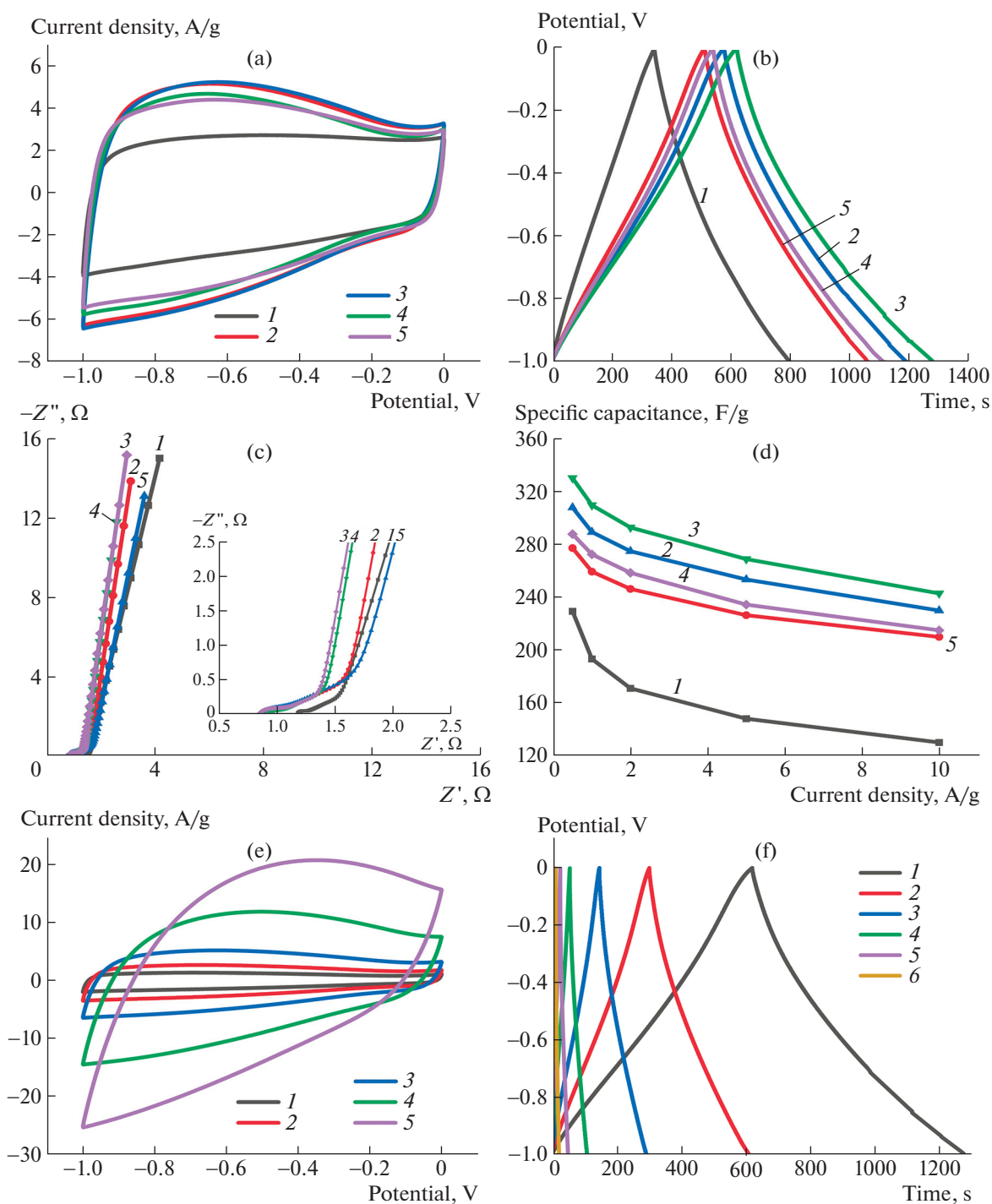
Fig. 7. (a) The CV curves (at 20 mV/s) of (*1*) Z8-C-800, (*2*) PZ-C-700, (*3*) PZ-C-800, (*4*) PZ-C-900, (*5*) PI-C-800. (b) the GCD curves (at 0.5 A/g) of (*1*) Z8-C-800, (*2*) PZ-C-700, (*3*) PZ-C-800, (*4*) PZ-C-900, (*5*) PI-C-800, (c) Nyquist plots and (d) the corresponding discharge capacitances of (*1*) Z8-C-800, (*2*) PZ-C-700, (*3*) PZ-C-800, (*4*) PZ-C-900, (*5*) PI-C-800. (e) The CV curves at (*1*) 5, (*2*) 10, (*3*) 20, (*4*) 50, (*5*) 100, mV/s. (f) The GCD curves of PZ-C-800 at (*1*) 0.5, (*2*) 1, (*3*) 2, (*4*) 5, (*5*) 10, (*6*) 20 A/g.

carried out, as shown in Fig. 7c. Figure 7c shows that the PZ-C-800 has a lower equivalent series resistance (*Rs*) of 0.85 Ω, which provides a conductive channel and favorable conditions for charge transfer [20]. In the lower frequency area, the slope is more steep, demonstrating that the spread resistance (Weber impedance) between carbon material and the electrolyte is less, so that electrolytes can easily reach the sur-
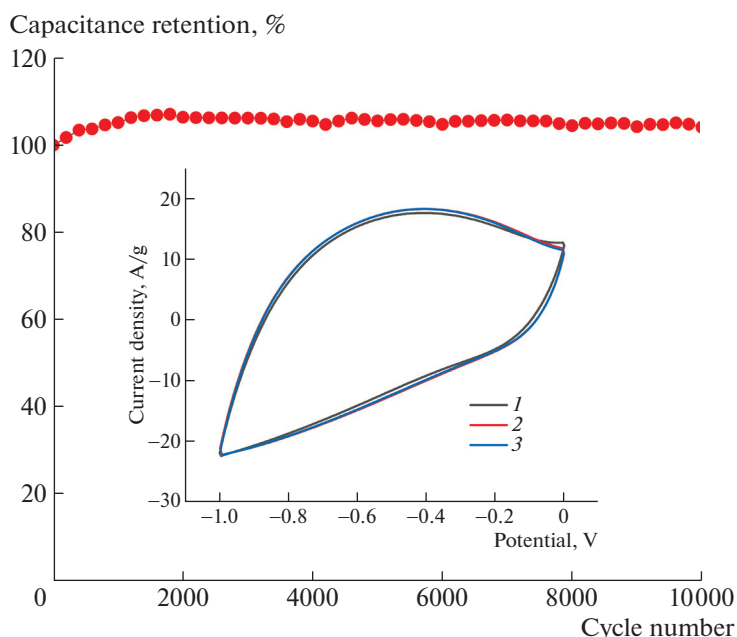
Fig. 8. Loop performance chart of PZ-C-800: (*1*) 1st, (*2*) 5000th, (*3*) 10000th.

face of the electrode. The slope of PZ-C-800 is the largest, indicating that the Weber impedance is shorter [22]. Figure 7d shows the specific capacitance values of PZ-C-800 are better than those of other carbon materials. when the scanning rate is 0.5 A/g, the PZ-C-800 can achieve a specific capacitance of 330.5 F/g. The PZ-C-800 exhibits strong multiplication performance, maintaining a capacitance retention of 73.5%. This is due to the fact that, after the introduction of ZIF-8, the N atoms in ZIF-8 are also retained under high-temperature carbonization. Thus, the amount of heteroatom doping is improved in PZ-C-800 compared to PI-C-800. High nitrogen-oxygen content provides good lubrication properties and electrochemically active points. So the electrolytes can quickly reach the surface of the material and the oxidation reaction can occur at the active location, which is conducive to the material maintaining a higher density than the capacitor at high current [30, 31]. Compared with the samples with different carbonization tem-

peratures, the 700°C carbonization is not sufficient, and the material has poorer electrical conductivity and specific surface area. The rate of carbonation at 900°C was too fast, resulting in a significant reduction in nitrogen content. And at 800°C, not only does this ensure the porous properties of the material, but the nitrogen content is also relatively high, so the PZ-C-800 performance is the best. Figure 7e shows the shape of the curves is slightly deformed with scan rate, but it still retains the rectangular. When the scanning rate reaches 100 mV/s, the curve remains well rectangular, showing good rate performance and proving it has good cycle stability. From Fig. 7f, the charging and discharging curves of PZ-C-800 exhibit a perfect isosceles triangle and no significant pressure drop. The results show that the material displays excellent charging and discharging characteristics, as well as excellent reversibility. This is due to the good nitrogen content and mechanical stability of the PZ-C-800. And when the scanning rate is 0.5 A/g, the discharge

Table 3. Comparison of the electrochemical properties of similar carbon materials

| Electrodes	Electrolytes	Energy/power density	Cycling stability, % (no. of cycles)	Refs.
Nitrogen-doped hierarchically porous carbon	0.5 M Na_2SO_4	14.4 W h/kg at 225 W/kg	93% (15000)	[16]
Lignin/PAN based carbon nanofibers	1 M Na_2SO_4	17.9 W h/kg at 800 W/kg	94.5% (5000)	[21]
Polyimide-based porous carbon nanoflowers	0.5 M Na_2SO_4	18.3 W h/kg at 500 W/kg	93.7% (10000)	[23]
Waste PI film-based porous carbons	1 M Na_2SO_4	13.2 W h/kg at 140 W/kg	100% (10000)	[31]
Nitrogen-oxygen co-doped porous carbon microspheres	1 M Na_2SO_4	20.5 W h/kg at 400 W/kg	82% (3000)	This work
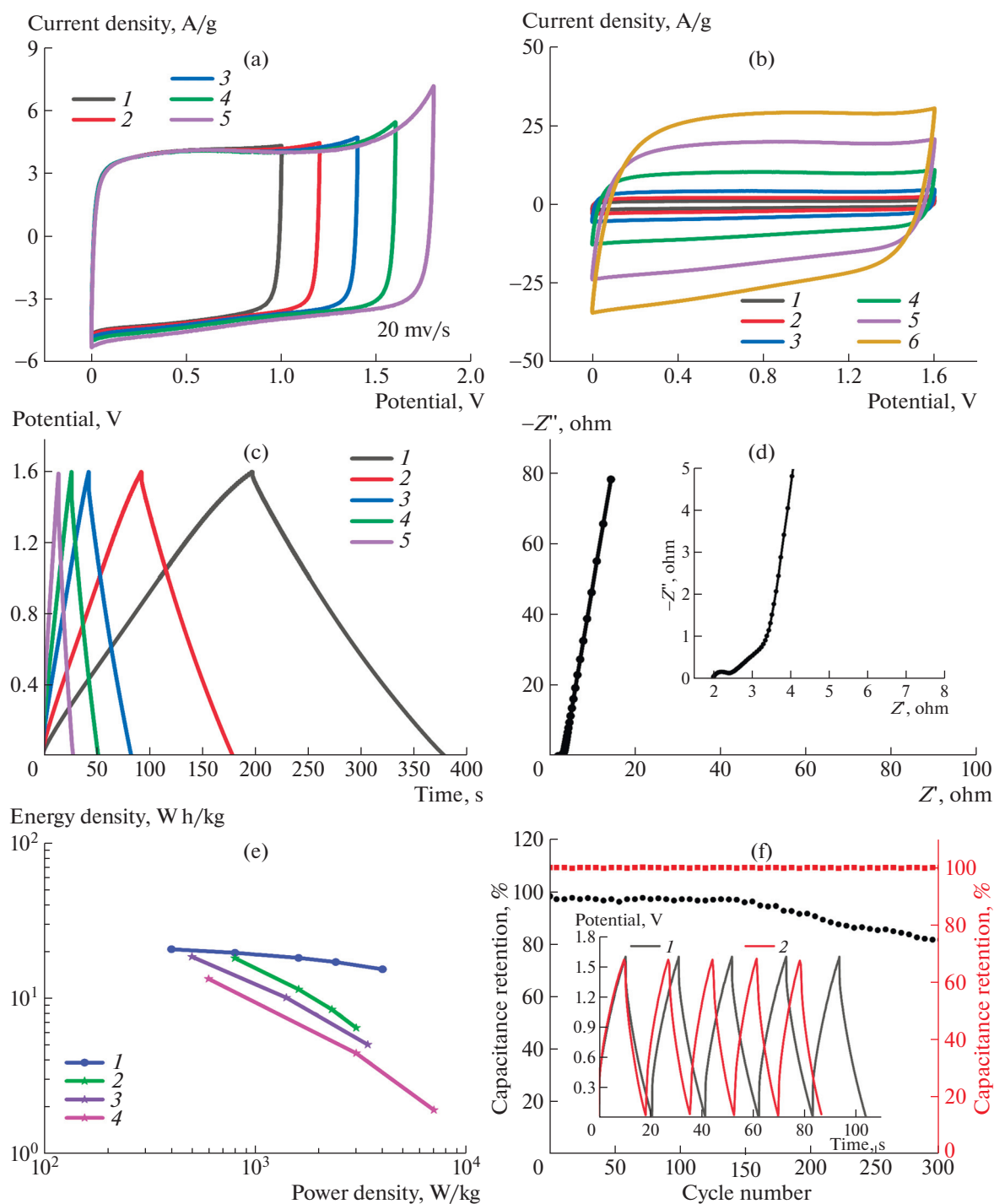
Fig. 9. (a) CV curves at different potential windows: (*1*) 1.0, (*2*) 1.2, (*3*) 1.4, (*4*) 1.6, (*5*) 1.8 V. (b) CV curves at (*1*) 5, (*2*) 10, (*3*) 20, (*4*) 50, (*5*) 100, (*6*) 150 mV/s. (c) GCD curves at (*1*) 0.5, (*2*) 1, (*3*) 2, (*4*) 3, (*5*) 5 A/g. (d) Nyquist plot. (e) Ragone plot: (*1*) this work, (*2*) [21], (*3*) [24], (*4*) [30]. (f) The cycling stability of the symmetrical supercapacitor: (*1*) first five cycles, (*2*) last five cycles.

time of the electrode material is about 660 s, indicating the better capacitive expression of the electrolyte.

After 10,000 cycles, the PZ-C-800 has a retention rate of 104%, meaning that the electrode material has good long-term electrochemical stability and is highly reversible, as shown in Fig. 8. The creation of oxygen functional groups on the carbon during the CV test by electrochemical oxidation may be the cause of the enhanced capacity, which activates more electrochemically active sites, increasing the double layer charge density, or generating redox reactions [32]. It

can also be seen from the illustration that the CV curve of the electrode material remains rectangular; the shape has not changed significantly, indicating that the capacity of the electrode has been adequately maintained.

In order to evaluate the usefulness of electrode material, a symmetrical supercapacitor was constructed. The symmetrical supercapacitor tested the performance of the sample with PZ-C-800 as both positive and negative poles, and 1 M Na_2SO_4 as an electrolyte. Figure 9a shows that its operating voltage window can be expanded to 1.8V, and the high working voltage allows the supercapacitor to store more energy, thereby increasing its energy density. Figure 9b displays the CV curve of the asymmetric supercapacitor under a 0−1.6 V voltage window. And the Figure 9b shows that the CV curve shape of the capacitor does not change significantly with the change in scanning rate and presents a rectangular shape. This indicates that the assembled asymmetric supercapacitor exhibits double electrical layer characteristics. In Fig. 9c, the GCD curves present an isosceles triangle, demonstrating that the devices possess excellent magnification performance and electrochemical reversibility. Figure 9d shows that the material has a low equivalent series resistance (Rs) of 2.1 Ω, which provides a conductive channel and favorable conditions for charge transfer. The line of the low-frequency region is almost vertical, demonstrating that the electrolyte has a small resistance to propagation in the electrode, which indicates that it has good electrochemical capacitor properties. In addition, the symmetric supercapacitors provide an energy density of 20.5 W h/kg at a power density of 400 W/kg, as shown in Fig. 9e. As shown in Fig. 9f, after 3000 cycles, the device still retains 82% of its initial value, demonstrating outstanding cycling stability. A comparison of the electrochemical properties of similar carbon materials is given in Table 3. It has been noticed that the PZ-C-800 symmetrical supercapacitor has a much greater energy density than the other materials. However, the long cycle life of this symmetrical supercapacitor needs to be improved.

CONCLUSIONS

In summary, porous carbon microspheres were successfully prepared through hydrothermal and carbonization processes using polyimide as the carbon source and ZIF-8 as the template. The prepared PZ-C-800 not only shows a sea urchin-like porous microsphere structure, but it also achieves co-doping of N and O. With 6 M KOH as the electrolyte, the specific capacitance of the PZ-C-800 electrode was 330.5 F/g at a scanning rate of 0.5 A/g, and the equivalent series Rs of the electrode was 0.85 Ω. The symmetrical supercapacitor, composed of two PZ-C-800 electrodes, attained an energy density of 20.5 W h/kg

at a power density of 400 W/kg when utilizing a 1 M Na_2SO_4 electrolyte. A novel technique for creating heteroatom-doped porous carbon materials for supercapacitors is presented in this work.

CONFLICT OF INTEREST

The authors of this work declare that they have no conflicts of interest.

REFERENCES

1. H. Peng, M. Zhang, K. Sun, X. Xie, H. Lei, and G. Ma, Appl. Surf. Sci. **529**, 147174 (2020).
2. S. Sardana, A. Gupta, K. Singh, A. S. Maan and A. Ohlan, J. Energy Storage **45**, 103510 (2022).
3. B. Yang, W. Zhang, and W. Zheng, Mater. Res. Lett. **11**, 517 (2023).
4. X. Chu, F. Meng, T. Deng, and W. Zhang, Nanoscale **13**, 5570 (2021).
5. Z. Pan, S. Yu, L. Wang, C. Li, F. Meng, N. Wang, S. Zhou, Y. Xiong, Z. Wang, Y. Wu, X. Liu, B. Fang, and Y. Zhang, Nanomaterials **13**, 1744 (2023).
6. S. Maji, R. Chaudhary, R. G. Shrestha, R. L. Shrestha, B. Demir, D. J. Searles, J. P. Hill, Y. Yamauchi, K. Ariga, and L. K. Shrestha, ACS Appl. Energ. Mater. **4**, 12257 (2021).
7. W. Tian, H. Zhang, X. Duan, H. Sun, G. Shao, and S. Wang, Adv. Funct. Mater. **30**, 1909265 (2020).
8. X. Zhang, W. Jian, L. Zhao, F. Wen, J. Chen, J. Yin, Y. Qin, K. Lu, W. Zhang, and X. Qiu, Colloids Surf., A **636**, 128191 (2022).
9. W. Du, Y. Bai, J. Xu, H. Zhao, L. Zhang, X. Li, and J. Zhang, J. Power Sources **402**, 281 (2018).
10. Y. Zhao, J. Liu, M. Horn, N. Motta, M. Hu, and Y. Li, Sci. Chin. Mater. **61**, 159 (2018).
11. X. Zhang, Q. Fan, H. Yang, H. Xiao, and Y. Xiao, New J. Chem. **42**, 17389 (2018).
12. M. Kim, X. Xu, R. Xin, J. Earnshaw, A. Ashok, J. Kim, T. Park, A. K. Nanjundan, W. A. El-Said, J. W. Yi, J. Na, and Y. Yamauchi, ACS Appl. Mater. Interfaces **13**, 52034 (2021).
13. Y. Cui, L. Zhao, C. Zhao, H. Yu, B. Zhao, X. Gu, J. Wang, L. Meng, and X. Gao, J. Mol. Struct. **1275**, 134643 (2023).
14. K. O. Otun, M. S. Xaba, S. Zong, X. Liu, D. Hildebrandt, S. M. El-Bahy, M. T. Alotaibi, and Z. M. El-Bahy, Colloid Interface Sci. Commun. **47**, 100589 (2022).
15. Y. Zheng, K. Chen, K. Jiang, F. Zhang, G. Zhu, and H. Xu, J. Energy Storage **56**, 105995 (2022).
16. R. Zhao, H. Peng, H. Wang, J. Liang, Y. Lv, G. Ma, and Z. Lei, J. Energy Storage **28**, 101174 (2020).
17. X. Yan, H. You, W. Liu, X. Wang, and D. Wu, Nanomaterials **9**, 1189 (2019).

18. F. Wang, L. Chen, H. Li, G. Duan, S. He, L. Zhang, G. Zhang, Z. Zhou, and S. Jiang, Chin. Chem. Lett. **31**, 1986 (2020).

19. M. Devi, S. Yesmin, B. Das, S. S. Dhar, and R. Dasgupta, Energy Fuels **37**, 3247 (2023).

20. Z. Liu, A. Qin, K. Zhang, P. Lian, X. Yin, and H. Tan, Nano Energy **90**, 106540 (2021).

21. R. Zhang, X. Jing, Y. Chu, L. Wang, W. Kang, D. Wei, H. Li, and S. Xiong, J. Mater. Chem. A **6**, 17730 (2018).

22. Z. Dai, P. Ren, W. He, X. Hou, F. Ren, Q. Zhang, and Y. Jin, Renewable Energy **162**, 613 (2020).

23. H. Peng, S. Qi, Q. Miao, R. Zhao, Y. Xu, H. Lei, F. Wang, G. Ma, and Z. Lei, J. Energy Storage **30**, 101493 (2020).

24. Y. Long, X. An, H. Zhang, J. Yang, L. Liu, Z. Tian, G. Yang, Z. Cheng, H. Cao, H. Liu, and Y. Ni, Chem. Eng. J. **451**, 138877 (2023).

25. Z. Shen, Y. Mo, J. Du and A. Chen, Appl. Surf. Sci. **527**, 146845 (2020).

26. L. Zhuo, S. Tang, K. Zhao, F. Xie, and Y. Bai, J. Appl. Polym. Sci. **137**, 48484 (2020).

27. Y. Kim, H. Park, and Y. Lee, J. Membr. Sci. **255**, 265 (2005).

28. Y. Liu, Q. Ren, S. Liang, L. Li, S. Wang, Z. Shi, Z. Pan, and T. Wang, ACS Appl. Energ. Mater. **5**, 1205 (2022).

29. Z. Sheng, L. Shao, J. Chen, W. Bao, F. Wang, and X. Xia, ACS Nano **5**, 4350 (2011).

30. F. Huang, G. Feng, J. Yin, S. Zhou, L. Shen, S. Wang, and Y. Luo, Nanomaterials **10**, 2547 (2020).

31. Y. Liu, H. Wang, C. Li, S. Wang, L. Li, C. Song, and T. Wang, Int. J. Energy Res. **46**, 370 (2022).

32. Z. Fan, Y. Liu, J. Yan, G. Ning, Q Wang, T. Wei, L. Zhi, and F. Wei, Adv. Energy Mater. **2**, 419 (2012).